T.Z.M. based on comparison of Galileo PPR and SSI data with the Calar Alto and Pic-du-Midi observations of impacts H and L by Hamilton *et al.* (*17*) and Drossart *et al.* (*18*).
24. J. C. Arvesen, R. N. Griffin Jr., B. D. Pearson Jr., *Appl. Opt.* **8**, 2215 (1969).
25. H. A. Weaver *et al.*, *Science* **267**, 1282 (1995).
26. This research was carried out by the Jet Propulsion Laboratory, California Institute of Technology, under a contract with the National Aeronautics and Space Administration. We acknowledge support from the Galileo Project. The impact timing predictions of P. Chodas and D. Yeomans were essential to the timing of the data acquisition.

2 December 1994; accepted 3 May 1995

Outburst of Jupiter's Synchrotron Radiation After the Impact of Comet Shoemaker-Levy 9

Imke de Pater,* C. Heiles, M. Wong, R. J. Maddalena, M. K. Bird, O. Funke, J. Neidhoefer, R. M. Price, M. Kesteven, M. Calabretta, M. J. Klein, S. Gulkis, S. J. Bolton, R. S. Foster, S. Sukumar, R. G. Strom, R. S. LePoole, T. Spoelstra, M. Robison, R. W. Hunstead, D. Campbell-Wilson, T. Ye, G. Dulk, Y. Leblanc, P. Galopeau, E. Gerard, A. Lecacheux

Jupiter's nonthermal microwave emission, as measured by a global network of 11 radio telescopes, increased dramatically during the Shoemaker-Levy 9 impacts. The increase was wavelength-dependent, varying from ~10 percent at 70 to 90 centimeters to ~45 percent at 6 and 36 centimeters. The radio spectrum hardened (flattened toward shorter wavelengths) considerably during the week of impacts and continued to harden afterward. After the week of cometary impacts, the flux density began to subside at all wavelengths and was still declining 3 months later. Very Large Array and Australia Telescope images of the brightness distribution showed the enhancement to be localized in longitude and concentrated near the magnetic equator. The evidence therefore suggests that the increase in flux density was caused by a change in the resident particle population, for example, through an energization or spatial redistribution of the emitting particles.

A worldwide network of radio telescopes was organized to observe Jupiter's flux density at microwave frequencies before, during, and after comet Shoemaker-Levy 9 (SL9) collided with the planet in July 1994. Our goal was to monitor Jupiter's microwave emission and to search for changes in the synchrotron radiation emitted by relativistic electrons (~1 to 300 MeV) trapped in Jupiter's inner magnetosphere.

The mechanism that produces the planet's steady synchrotron radiation is well understood, and the observed radiation characteristics were used in the early 1960s to derive Jupiter's magnetic field configuration and electron distributions (*1*). Jupiter's radio emission has been monitored continuously since the early 1970s at 13 cm (*2*). The flux density varies smoothly between ~3.5 and 5 Jy (1 jansky = 10^{-26} W m^{-2} Hz^{-1}), over time scales of years. Although short-term time variability (days) in the flux density has been reported more than once (*1*), it has never been confirmed (*3*). During a jovian rotation, the flux density displays a sinusoidal variation in amplitude, commonly referred to as the "beaming curve" (Fig. 1). The peak-to-peak amplitude in the beaming curve is ~15%. The variation with jovian rotation of all radiation characteristics (in particular, the polarized components) implied a misalignment between the magnetic and rotational axes of ~10° and a confinement of most radiating electrons to the planet's magnetic equator (*1*).

It is usually assumed that electrons, on average, diffuse inward in Jupiter's magnetosphere while the first adiabatic invariant is conserved. Hence, the particles gain energy in the diffusion process, and they lose it by synchrotron radiation. As the electrons move through the magnetosphere, they interact with solid material such as moonlets and dust, electromagnetic waves, and neutral and charged particles. All interactions usually result either in a loss of the electron or in a reduction in its energy (*4*).

Predictions before the event had concentrated on the interaction of the radiating electrons with cometary dust (*5, 6*). It was suggested that the radio emission would decrease as a result of energy degradation by cometary dust. This decrease would be most apparent at low frequencies. The highlight of the radio observations instead was a dramatic increase in the radio flux density during the 6 days of cometary bombardment. The increase in radio brightness was monotonic at a roughly constant rate during the week of impacts. Data taken during a 3-month period after the week of cometary impacts showed a steady decline in the radio flux density; by the end of October 1994, equilibrium had not yet been reached at the short wavelengths.

We observed Jupiter's radio emission between June and October 1994, with 11 different radio telescopes (single dishes and arrays of telescopes) (Table 1). We restricted our attention to total flux densities obtained at wavelengths between 6 and 90 cm (*7*). We calibrated all data against 3C286, either directly, or indirectly by means of a nearby secondary calibrator source (*8*). Although we also searched for burstlike emission (time scales varying from microseconds to seconds), no obvious activity or "radio bursts" could be associated with the times of impact events.

With the single dish telescopes, we determined the total flux density S of the planet either by scanning the planet in one (Nançay) or two (orthogonal) directions (Green Bank, Effelsberg, and Parkes) or by doing on-off scans (DSN and NRL) (see Table 1 for telescope abbrevations). Because the spatial extent of Jupiter's radio

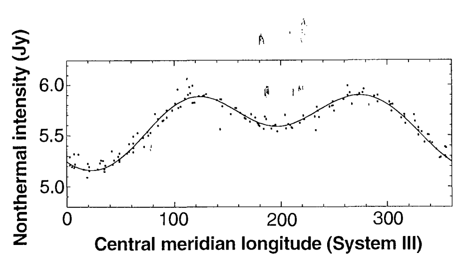

Fig. 1. A preimpact beaming curve (wavelength, 20 cm) of Jupiter's synchrotron radiation. The data were taken with the 140-foot NRAO telescope at Green Bank. Superposed is a best fit line after Eq. 1.

I. de Pater, C. Heiles, M. Wong, Astronomy Department, University of California, Berkeley, CA 94720, USA.
R. J. Maddalena, National Radio Astronomy Observatory, Green Bank, WV 24944, USA.
M. K. Bird and O. Funke, Universität Bonn, 53121 Bonn, Germany.
J. Neidhoefer, Max-Planck-Institut für Radioastronomie, 53121 Bonn, Germany.
R. M. Price, M. Kesteven, M. Calabretta, Commonwealth Scientific and Industrial Research Organization, Epping, New South Wales 2121, Australia.
M. J. Klein, S. Gulkis, S. J. Bolton, Jet Propulsion Laboratory, Pasadena, CA 91109, USA.
R. S. Foster, Naval Research Laboratory, Code 7210, Washington, DC 20375, USA.
S. Sukumar, Dominion Radio Astrophysical Observatory, National Research Council, Penticton, British Columbia V2A 6K3, Canada.
R. G. Strom and T. Spoelstra, Netherlands Foundation for Research in Astronomy, Post Office Box 2, 7990 AA Dwingeloo, Netherlands.
R. S. LePoole, Leiden University, Post Office Box 9513, 2300 RA Leiden, Netherlands.
M. Robison, New Mexico Institute of Mining and Technology, Socorro, NM 87801, USA.
R. W. Hunstead, D. Campbell-Wilson, T. Ye, School of Physics, University of Sydney, New South Wales 2006, Australia.
G. Dulk, Astrophysical, Planetary, and Atmospheric Sciences, Boulder, CO 80309, USA.
Y. Leblanc, P. Galopeau, E. Gerard, A. Lecacheux, Observatoire de Paris, 92195 Meudon, France.

*To whom correspondence should be addressed.

emission is a nonnegligible fraction of the beam width of the Effelsberg (6 and 11 cm) and DSN (13 cm) telescopes, the recorded peak flux density had to be corrected. For an extended uniform disk, applicable for Jupiter's thermal emission, the correction factor C_d can readily be determined (9) to have values typically ~1.02 at 6 cm and less than 1.01 at 11 to 13 cm. We divided the expected thermal flux density by C_d to obtain the "observed" thermal flux density, S_t. We assumed S_t = constant (see below). The total observed nonthermal flux density, S_{nt}, is then given by $S_{nt} = S - S_t$. To correct for the decrease in intensity in S_{nt}, this quantity was multiplied by a factor C_{nt}, determined empirically from 90-cm VLA and WSRT images (10). Corrections to the data over the period June through October 1994 were typically C_{nt}(6 cm) ≈ 1.2 to 1.3, C_{nt}(11 cm) ≈ 1.04 to 1.14, and C_{nt}(13 cm) ≈ 1.02 to 1.05.

At long wavelengths, particularly above ~30 cm, it becomes increasingly difficult to determine total flux densities with single-element telescopes (11). We therefore determined Jupiter's total flux density at these wavelengths by imaging the planet using interferometry. This allowed us to distinguish Jupiter from background radio sources and to determine the rotation-averaged flux density for the planet (12).

We attribute the increase and subsequent decrease in Jupiter's total flux density to variations in its nonthermal flux density. Evidence for this assumption is based on the following observations: (i) VLA and AT reports on Jupiter's thermal brightness distribution at wavelengths of 3.6 and 6 cm (13) showed no changes during the SL9 impacts. (ii) Simultaneously with the observed increase in Jupiter's total intensity, the relative linear polarization increased by ~2% at wavelengths of 11 and 20 cm (14).

To facilitate comparison among the different wavelengths, we focused on the nonthermal flux density. We corrected all data for the planet's thermal contribution by subtracting a flux density corresponding to a disk temperature of 350 K at 20 cm, 280 K at 11 cm, and 230 K at 6 cm (15), interpolated or extrapolated to other wavelengths. All observed flux densities were scaled to the standard geocentric distance of 4.04 astronomical units (AU).

To best determine the variations in Jupiter's synchrotron radiation, we modeled the beaming curve (Fig. 1) according to

$$S = S_0 + S_1 + S_2 \sum A_n \sin[n(\lambda_{III} + \lambda_n)] \qquad (1)$$

where S is the observed flux density (corrected for telescope resolution effects as outlined above) at jovian System III (1965.0) central meridian longitude λ_{III}; S_0 is the thermal contribution; and S_1, S_2, A_n, and λ_n are constants to be fitted for $n = 1$, 2, and 3 (1, 2). The shape of the beaming curve is constant over time, except for changes in the viewing geometry resulting from variations in the jovian declination of Earth (2). Because observations of Jupiter in the Northern Hemisphere covered only a fraction of a jovian rotation, we assumed that the shape of the beaming curve remained constant for measurements made during and after the week of cometary impacts (16). The parameters A_n and λ_n were determined from full preimpact beaming curves at each frequency; we then determined both S_1 and S_2 by fitting the data during and after the week of impacts. The

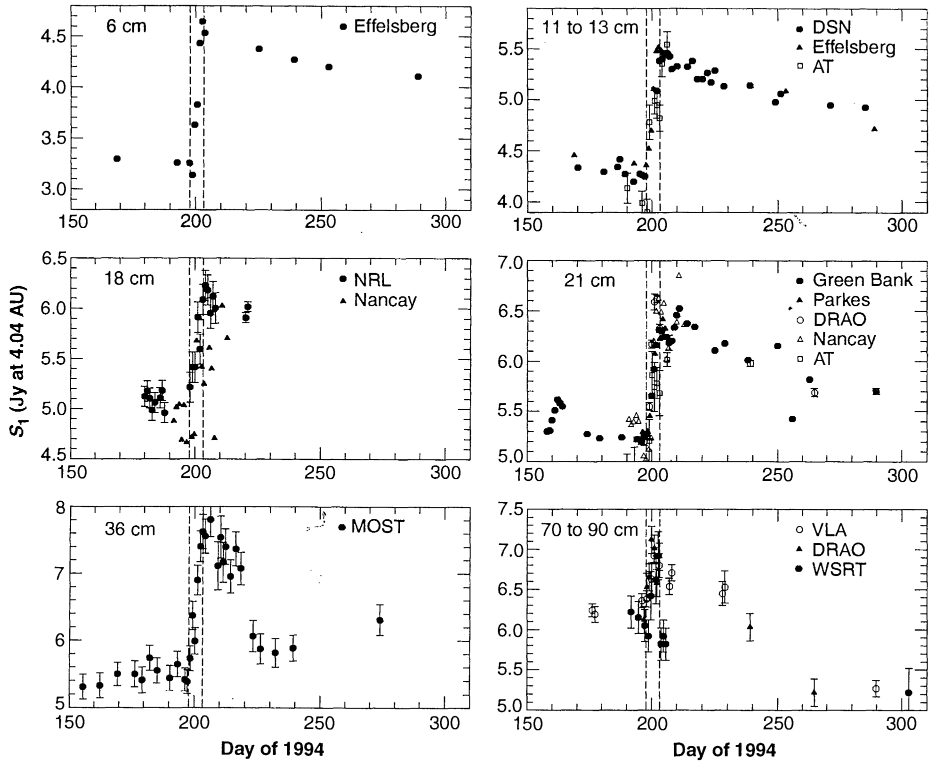

Fig. 2. Jupiter's nonthermal flux density is plotted as a function of 1994 day of year, at wavelengths 6, 11 to 13, 18, 21, 36, and 70 to 90 cm (S_1 from Eq. 1). The average value of the 1370- and 1480-MHz Green Bank data is shown. The 20-cm DRAO data were 8% lower than the Green Bank data. This is attributed to (unknown) pointing errors. All DRAO data were multiplied by a factor of 1.08 to crudely correct for this effect. At 21 cm, only the Green Bank and Parkes data were used to determine the overall increase in flux density during the week of cometary impacts. None of the data shown are corrected for background radio confusion. Background confusion is particularly strong at 21 cm near day 210. Preliminary background experiments and two-dimensional images obtained with the various interferometers suggest the presence of a source with a flux density of ~0.2 Jy at 21 cm on this day. [The data will be corrected for confusion (26).] The dashed lines show the times of the first (fragment A) and last (fragment W) impacts.

Fig. 3. The evolution of Jupiter's spectrum. Spectra are shown for the time before the week of cometary impacts, at the end of the impact week (21 July), and a few months after the impacts (early October). The straight lines are least square fits to the data points, at frequencies above and below 1.3 GHz (wavelength, 20 cm) for the preimpact data and at frequencies above and below 0.84 GHz (wavelength, 36 cm) for the data after the impacts.

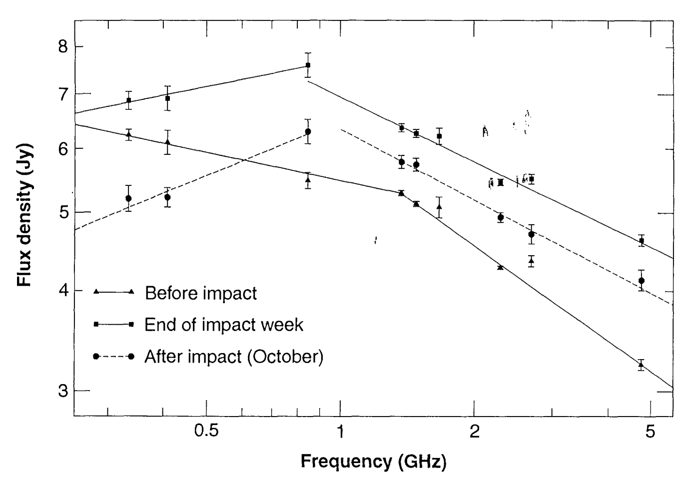

changes in the total nonthermal flux density are well represented by the S_1 values.

The quantity S_1 from Eq. 1 (Fig. 2) shows a clear, steady increase in intensity during the week of cometary impacts from day 198 (17 July) to day 203 (22 July). The fractional increase in intensity is wavelength-dependent: 10 to 13% at 90 to 70 cm, 20 to 22% at 22 to 18 cm, 25 to 26% at 13 to 11 cm, and 43% at 6 cm, with a notable anomaly of 39 ± 7% at 36 cm. Because radiation from higher energy electrons is emitted at shorter wavelengths, the data suggest that the spectrum of radiating electrons hardened during the week of cometary impacts (Fig. 3). After the week of the SL9 impacts, the flux density began to subside at all wavelengths; the flux density at 70 to 90 cm, however, started to decline before the end of the impact week, about 2 days earlier than at other wavelengths. The radio spectrum from above ~30 cm continued to harden after the week of SL9 impacts. Three months after the impacts, the radiation levels were still declining at the shorter wavelengths.

The VLA and AT images of Jupiter taken before and during the week of cometary impacts show that the brightness distribution of Jupiter's synchrotron radiation changed significantly during the week of cometary impacts. The 20-cm VLA images (Fig. 4) are 20-min snapshot observations centered at $\lambda_{III} \approx 110°$. The 13-cm AT images (Fig. 5), although formed from continuous 11-hour observations, are weighted most heavily toward $\lambda_{III} \approx 60°$ (*17*). Both sets of images show a dramatic local enhancement in the radiation belts, concentrated near the magnetic equator. As observed at $\lambda_{III} \sim 60°$ and 110°, it is almost exclusively the left side of the belt that has changed; that side has brightened considerably and has moved inward by $\sim 0.2R_J$ (VLA image; $1R_J$ is one jovian radius).

It seems implausible that the excess radiation is caused by particle injection from the impact site because such particles would most likely end up at the conjugate foot point of the field line emanating from the impact site. Such precipitating particles may well be responsible for the ultraviolet and x-ray emissions detected at northern mid-latitudes during and after the impact of fragment K (*18*). We suggest that the increase in radio flux density was caused by a change in the resident particle population, as a result, for example, of an energization or spatial redistribution of the emitting particles.

An enhancement in radial diffusion would increase the radio emission (*19*, *20*). It was suggested that cometary impacts could trigger an increase in radial diffusion, either globally or locally (*21*). An increase in the diffusion coefficient would lead to an inward displacement of the radiation peaks. Suppose an increased radial diffusion causes the radiation peaks to shift inward by $0.05R_J$ from the nominal (preimpact) peak at $1.45R_J$

Table 1. Telescopes participating in the Jupiter SL9 radio observation campaign.

Telescope location*	Type, size	Frequency (MHz)	Bandwidth (MHz)
NRAO 140-foot telescope Green Bank)	Single dish, 43 m	1370 1480	40 40
MPIR 100-m telescope (Effelsberg)	Single dish, 100 m	2695 4750 10550†	200 500 300
Parkes Radio Telescope	Single dish, 64 m	1404	64
NASA DSN (DSS 13/14)	Single dishes, 34 and 70 m	2295	20
Nançay Telescope	Transit telescope, 200 m by 35 m	1404, 1416 1664, 1668 3263, 3335†	2 × 6.4 2 × 3.2 2 × 6.4
NRL	Single dish, 26 m	1665	50
WSRT	East-west array, seven 25-m dishes per frequency Spacings: 144 m to 2.8 km	1400† 326	8 × 5 5
AT	East-west array, six 22-m dishes Spacings: 70 m to 6 km	1380 2378	160 160
MOST	East-west array, two collinear cylindrical paraboloids Spacings: 15 m to 1.6 km	843	3
VLA	Y-shaped array, 27 25-m dishes Spacings: 250 m to 10 km	1365† 330	50 3
DRAO	East-west array, seven 9-m dishes Spacings: 12.9 to 604 m	1420 408	30 4

*NRAO, National Radio Astronomy Observatory, Green Bank, WV, USA; MPIR, Max-Planck-Institut für Radioastronomie, Effelsberg, Germany; Parkes Radio Telescope, Parkes, Australia; NASA DSN (DSS 13/14), NASA Deep Space Network, Goldstone, CA, USA; Nançay Telescope, Nançay, France; NRL, Naval Research Laboratory, Nanjemoy, MD, USA; WSRT, Westerbork Synthesis Radio Telescope, Westerbork, Netherlands; AT, Australia Telescope, Narrabri, Australia; MOST, Molonglo Synthesis Telescope, Canberra, Australia; VLA, Very Large Array of the NRAO, Socorro, NM, USA; DRAO, Dominion Radio Astrophysical Observatory, Penticton, Canada. †Not reported here.

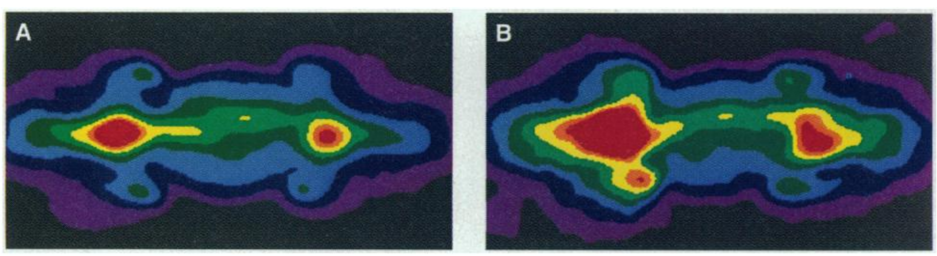

Fig. 4. VLA 20-cm radio images of Jupiter at $\lambda_{III} \approx 110°$ at two 1994 UT dates: (**A**) 24 June 03:00 UT (before the comet impacts) and (**B**) 20 July 03:00 UT (during the impact week). The two images are on the same color intensity scale; both are rotated on the sky so that the magnetic equator is horizontal on the figure. The peak value in the 20 July image is approximately 2500 K; in the 24 June image, it is approximately 1700 K. The full beam width at half power is approximately $0.3R_J$.

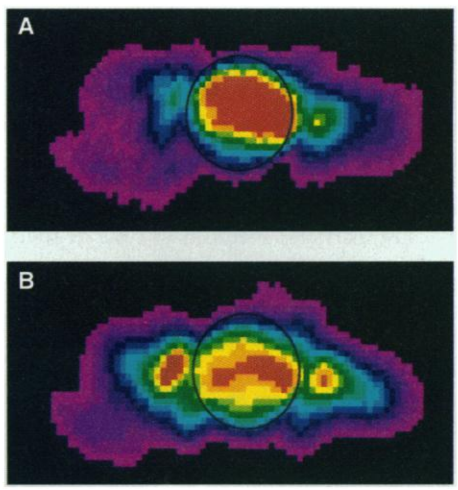

Fig. 5. AT radio images at 13 cm at $\lambda_{III} \approx 60°$ (**A**) 15 July 02:00 to 13:00 UT (before the impacts) and (**B**) 20 July 02:00 to 13:00 UT (during the impact week). The two images are on the same color intensity scale; both are rotated on the sky so that the magnetic equator is horizontal on the figure. The maximum intensity is 450 K. The full beam width at half power is approximately $0.21R_J$ by $1.0R_J$, with the long axis at position angle PA ≈ −20°.

(22). The magnetic field strength B at $1.40R_J$ is 1.11 times that at $1.45R_J$. The electrons gain energy while diffusing inward through conservation of the first adiabatic invariant (E^2/B = constant, where E is the electron's energy). Because the observing frequency ν does not change ($\nu \sim E^2B \rightarrow E^2B$ = constant), the radiating electron population at $1.40R_J$ is different from that at $1.45R_J$: We effectively receive radiation from electrons with energies lower by a factor of 1.11 than those radiating at $1.45R_J$. Because there are more low-energy electrons and because the magnetic field strength seen by the particles increased as a result of the inward radial displacement, the synchrotron radiation increases: $S \sim N(E)B$, where $N(E)$ is the electron density at energy E. If Jupiter's radio spectrum follows a simple power law of the form $S \sim \nu^{-\alpha}$, the fractional increase in flux density would be equal at each wavelength, λ. However, the preimpact spectral index α was ~0.10 at $\lambda \gtrsim 20$ cm and was ~0.4 at $\lambda \lesssim 20$ cm [Fig. 3; (22)]. Such a spectrum would lead to a ~33% increase in flux density at the short wavelengths and an increase of ~25% at longer wavelengths. An enhancement in radial diffusion would thus result in an increase in the radio emission and a hardening of the radio spectrum. Although more detailed calculations need to be performed, given the observed changes in Jupiter's flux density and radio spectrum (relative increases of ~10% at 90 cm, 20 to 25% at 10 to 20 cm, and ~40% at 6 and 36 cm), we believe it is unlikely that this mechanism alone can be fully responsible for the observed changes in the radio flux densities and spectrum.

It has also been suggested that pitch angle scattering of the resident particle population by whistler-mode waves might broaden the pitch angle distribution (23), resulting in an increase in synchrotron radiation. In this scenario, electrons in the magnetic equator are pitch angle–scattered such that they mirror at higher latitudes, where the magnetic field strength is greater. Because particles spend most time at their mirror points, the radio intensity as well as the spatial extent in latitude of the emitting region would be increased. In contrast to the radial diffusion model outlined above, according to this model the electrons may not be energized. If pitch angle scattering is energy-independent, the radio flux density may increase significantly, but the radio spectrum will not harden as much as in the radial diffusion model. However, wave particle interactions generally do depend on energy, and detailed calculations are necessary to predict the resulting radio spectrum.

An alternative model (24) is that energization of the resident electron population takes place by a collisionless magnetohydrodynamic (MHD) shock, triggered by the cometary impacts. Low-energy electrons are accelerated, resulting in a net gain of high-energy electrons at the expense of low-energy particles. In addition to being energized, electrons are scattered in pitch angle, and radial diffusion is triggered by induced electric fields. The MHD shock model requires a localized source and leads to energy-dependent energization. Numerical calculations (24) show a remarkable similarity to the observations at 6, 11 to 13, 20, and 90 cm.

After the week of cometary impacts, the particle distribution was expected to relax, resulting in a decrease in the radio emission. The relaxation time depends on the diffusion process, and it may take half a year before a (new) equilibrium level is reached (5, 20). Hence, it is not surprising that the radio emission was still decreasing 3 months after the impacts.

The dust density in Jupiter's magnetosphere was expected to increase because of the passage of SL9 (25). The interaction of Jupiter's energetic electron population with this cometary dust was investigated by several researchers (5, 6). Micrometer-sized dust degrades an electron's energy by $3a$ MeV, where a is the radius of the grain in centimeters (grain density of 1 g cm^{-3}). The relative energy loss will be greatest for low-energy electrons, resulting in a hardening of Jupiter's radio spectrum. Whereas hardening during the week of the SL9 impacts must be caused primarily by processes triggered by the impacts, the hardening after the week of impacts may, in part, be caused by degradation effects from cometary dust. A comparison of the data with model calculations (5) suggests the cometary dust density to be less than 10^{-6} cm^{-3}.

The comet impact has provided us with a unique experiment to unravel one of the outstanding issues in magnetospheric physics: the energization and radial transport mechanism of the energetic electrons in Jupiter's radiation belts. It will be necessary to continue monitoring the planet at radio wavelengths to determine (i) when a new equilibrium in the flux density levels is reached and if this is wavelength-dependent, and (ii) the flux density level and spectral index after equilibrium has been reached. This information is crucial for determining whether radial diffusion is the main mode of particle transport and, if so, how fast particles are transported (the value of the radial diffusion coefficient) and whether this process is energy-dependent. Continuous monitoring is also necessary to determine how much cometary dust has been trapped in Jupiter's inner magnetosphere.

REFERENCES AND NOTES

1. I. de Pater and M. J. Klein, in "Time Variable Phenomena in the Jovian System," *NASA P-494*, M. S. Belton *et al.*, Eds., p. 139, and references therein.
2. M. J. Klein, T. J. Thompson, S. Bolton, *ibid.*, p. 151. Equation 1 in this report is slightly different from the version used in earlier work.
3. S. J. Bolton, thesis, University of California, Berkeley (1991).
4. I. de Pater and C. K. Goertz, *J. Geophys. Res.* **95**, 39 (1990).
5. I. de Pater, *Geophys. Res. Lett.* **21**, 1071 (1994).
6. A. J. Dessler and T. W. Hill, *ibid.*, p. 1043; W.-H. Ip, *Planet. Space Sci.* **42**, 527 (1994).
7. Many data sets also contain information on the polarization characteristics and on the brightness distribution of the emission. This information will be reported elsewhere.
8. J. W. M. Baars, R. Genzel, I. I. K. Pauliny-Toth, A. Witzel, *Astron. Astrophys.* **61**, 99 (1977); updated by M. Ott *et al.*, *ibid.* **284**, 331 (1994). The secondary calibrator sources 1508-055, 1127-145, and 1308-220 were used to intercalibrate the data from Green Bank, DSN, Effelsberg, Parkes, MOST, and the VLA.
9. B. L. Ulich and R. W. Haas, *Astrophys. J. Suppl. Ser.* **30**, 247 (1976).
10. At a wavelength of 90 cm, the thermal contribution is negligible (~1%), and both the VLA and WSRT arrays received all of the emission. We determined C_{nt} by convolving the 90-cm images down to the resolution of the single dish telescope, the peak in the convolved images being equal to the value recorded by a single dish. These empirically determined curves of C_{nt} as a function of single dish half-power beam width will be published separately, together with the VLA and WSRT data (I. de Pater *et al.*, in preparation).
11. The field of view of a telescope is proportional to λ/D, where λ is the observing wavelength and D is the diameter of the telescope. Hence, at long wavelengths the field of view increases substantially and with it the background radio noise. Furthermore, both the total number of radio sources and their intensities increase dramatically with increasing wavelength [A. G. Willis *et al.*, *Int. Astron. Union Symp.* **74**, 39 (1977)].
12. The interferometer data were generally reduced according to the following procedure: After the spatial frequency (ultraviolet) data were edited and calibrated, they were gridded and Fourier-transformed to give maps of the object. In the case of the low-frequency data (70 to 90 cm), a large map (3° to 5°) was produced on which background sources could be identified. In some data sets (VLA and WSRT), these sources were then subtracted, and new maps were produced "free" of background radio sources. Depending on the beam size, the data were then "corrected" for the up-and-down motion of the radiation belts on the sky during a jovian rotation, caused by the misalignment of the magnetic and rotation axes. Self-calibration helped improve the phases of the final data sets. The rotation-averaged flux density was then determined from the final images (heavily tapered where appropriate).
13. A. W. Grossman *et al.*, *Bull. Am. Astron. Soc.* **26**, 1587 (1994).
14. The degree of linear polarization was found to increase during the week of SL9 impacts with the Effelsberg (11 cm), Green Bank (20 cm), and Parkes (20 cm) telescopes. A preliminary report was given by M. K. Bird, O. Funke, J. Neidhoefer, and I. de Pater [*Int. Astron. Union Circ. 6069* (1994)].
15. I. de Pater, *Annu. Rev. Astron. Astrophys.* **28**, 347 (1990).
16. Although the shape of the beaming curve has not changed over the past 20 years (except for changes due to the changing viewing geometry of the planet), the beaming curves did change considerably during and after the week of impacts; these changes were caused by large changes in Jupiter's spatial brightness distribution [I. de Pater, C. Heiles, M. Wong, R. J. Maddalena, *Int. Astron. Union Circ. 6074* (1994)]. We estimate the effect of beaming curve departures on S_1 to be less than 1 to 2%.
17. The AT images were constructed from 11 hours of observations, on 15 and 20 July between approximately 02:00 and 13:00 UT (universal time). The data are weighted most heavily to the extreme hour angles (that is, the first and last hour) because Jupiter's rotation period is 10 hours, so the first and last hour

cover the same λ_{III} range; moreover, the ultraviolet spacings at the extreme hour angles give the north-south resolution and have the appropriate spatial scales to record the major structures of Jupiter's radiation belts. The λ_{III} assigned to the images is therefore that of the extreme hour angles. The difference between the images of 15 and 20 July reflects the changes that occurred to the range longitudes to which the instrument is sensitive. The left side of the belt is much brighter than the right side. This agrees with the sequence of VLA images taken on 19 and 20 July (by I. de Pater *et al.*, in preparation). The AT images are reported by Y. Leblanc and G. A. Dulk, *Geophys. Res. Lett.*, in press; G. A. Dulk, Y. Leblanc, R. W. Hunstead, *ibid.*, in press.

18. J. H. Waite Jr. *et al.*, *Science*, in press; J. T. Clarke *et al.*, *ibid.* **267**, 1302 (1995).
19. N. M. Brice and T. R. McDonough, *Icarus* **18**, 206 (1973).
20. I. de Pater and C. K. Goertz, *J. Geophys. Res.* **99**, 2271 (1994).
21. W.-H. Ip, *Eos* **75** (fall suppl.), 404 (1994); *Planet. Space Sci.*, in press; A. J. Dessler and T. W. Hill, *Bull. Am. Astron. Soc.* **26**, 1593 (1994); T. Hill and A. J. Dessler, *Eos* **75** (fall suppl.), 402 (1994).
22. I. de Pater, *Astron. J.* **102**, 795 (1991).
23. S. J. Bolton, M. J. Klein, S. Gulkis, R. M. Thorne, R. Foster, *Eos* **75** (fall suppl.), 405 (1994).
24. S. H. Brecht, M. E. Pesses, J. G. Lyon, N. T. Gladd, S. W. McDonald, *Geophys. Res. Lett.*, in press; S. H. Brecht, M. E. Pesses, I. de Pater, N. T. Gladd, J. G. Lyon, *ibid.*, in press.
25. M. Horanyi, *ibid.* **21**, 1039 (1994).
26. M. Wong *et al.* in preparation.
27. This research was supported in part by National Science Foundation grant 22122 and National Aeronautics and Space Administration (NASA) grant NAGW-3917 to the University of California, Berkeley. The Westerbork telescope is operated by the Netherlands Foundation for Research Astronomy with financial support from the Netherlands Organization for Scientific Research (NWO). The VLA and the 140-foot telescope at Green Bank are part of the National Radio Astronomy Observatory, which is operated by Associated Universities, Inc., under a cooperative agreement with the National Science Foundation. The AT is operated by the Australia Telescope National Facility, CSIRO. The MOST is supported by grants from the Australian Research Council, the University of Sydney Research Grants Committee, and the Science Foundation for Physics within the University of Sydney. The Naval Research Laboratory's Maryland Point Observatory is supported by the Office of Naval Research and through an interagency agreement with NASA. The Dominion Radio Astrophysics Observatory synthesis telescope is operated by the National Research Council of Canada as a national facility. A portion of the work was performed by the Jet Propulsion Laboratory under contract with NASA.

19 December 1994; accepted 1 May 1995

Observation of Individual Chemical Reactions in Solution

Maryanne M. Collinson* and R. Mark Wightman†

Discrete chemical reaction events occurring in solution have been observed by single photon detection of a bimolecular, chemiluminescent reaction. The reactants were generated from 9,10-diphenylanthracene in acetonitrile with potential pulses applied to an ultramicroelectrode. Electrogenerated radical ions of opposite sign react to yield the excited singlet state of the parent compound. The chemical reactions were restricted to a 20-femtoliter volume adjacent to the electrode by the use of rapid potential pulses. Individual chemical reaction events were stochastic and followed the Poisson distribution, and the interarrival time between successive reaction events was exponentially distributed.

At a microscopic level, bimolecular chemical reactions generate products as a result of the collision of individual molecules. Normally, however, chemical reactions in solution are viewed as an ensemble of events, and the fluctuations associated with individual molecular collisions and their reactions are not observed. This is because both the location and time of an individual reaction event are usually undefined as a result of diffusion and encounter of the reagents before the reaction. In the gas phase, individual reactions can be examined because methods exist for exquisite control of delivery of reactants (*1*). In solids, the immobile nature of individual molecules allow their examination by near-field scanning microscopy (*2*) and laser spectroscopy (*3*). Although such approaches cannot be used for chemical reactions in fluids, we show that single reactions can be observed by restricting the volume occupied by the reactants and the observation time. This approach is similar to that used for solution-phase single molecule detection where molecules are spatially restricted in microdroplets (*4*), a thin flow cell (*5*), or at the focal point of a confocal microscope (*6*), and then temporally interrogated through laser-induced fluorescence (LIF). In this work, the solution reagents are restricted to a microscopic volume by electrogeneration with a microelectrode (*7*). The reagents undergo a chemiluminescent (CL) reaction (*8*) whose photon emission is time resolved with a multichannel scaler. This experiment reveals the stochastic nature of molecular reactions in solution and enables observation of the rates of chemical reactions at the level of individual events.

Introduction of 9,10-diphenylanthracene (DPA) in an acetonitrile solution into an electrochemical cell containing a microelectrode (*9*) pulsed between potentials sufficient to alternately generate its radical cation and radical anion results in chemiluminescence (Fig. 1A). The emission occurs predominantly during the shorter (50 μs) cathodic pulse (Fig. 2) as the electrogenerated radical anion diffuses into the sea of DPA radical cations generated in the 500-μs interval before the cathodic pulse. When the radical ions of opposite charge encounter each other, they react by electron transfer reaction to form either the nonemitting triplet state of DPA or the excited singlet state that relaxes to the ground state by photon emission (*10*). These events occur in a region adjacent to the electrode that has a volume of ~20 femtoliters defined by the electrode area (9×10^{-7} cm^2) and the distance an electrogenerated ion can diffuse from the electrode surface during the 50-μs step.

When the photons are counted over 1-s intervals, no evidence for individual reaction events is observed. The ensemble av-

Department of Chemistry, University of North Carolina, Chapel Hill, NC 27599–3290, USA.

*Present address: Department of Chemistry, Kansas State University, Manhattan, KS 66506–3701, USA.
†To whom correspondence should be addressed.

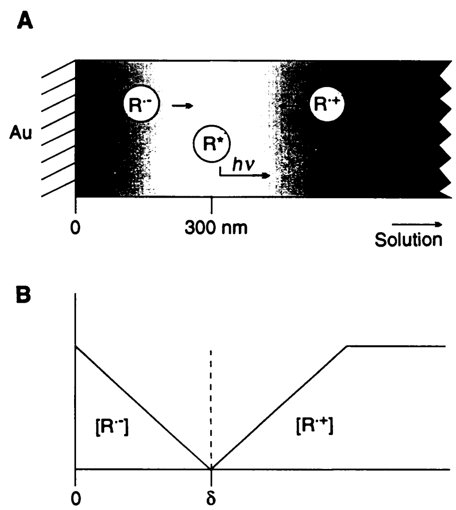

Fig. 1. Schematic diagram of the chemical reaction. (**A**) A radical anion (R·−) of 9,10-diphenylanthracene (DPA) is electrogenerated at a gold electrode during the cathodic potential pulse. It diffuses away from the electrode and encounters a radical cation (R·+) electrogenerated during the preceding time interval in which the electrode was maintained at a positive potential. The singlet-excited state of DPA (R*) is generated as a result of electron transfer between the two reactants. Photon emission leads to detection of the single chemical reaction. (**B**) Concentration profiles of the reactants for high concentrations of precursor as described by Eq. 2 (see text). Under this condition, the photon emission arises from a sharp plane at the intersection of the concentration profiles located a distance δ from the electrode surface.